Hybrid dual-mode tunable polarization conversion metasurface based on graphene and vanadium dioxide

JIAXING FANG,[1,2] WEI ZHU,[1,3] LIN CAO,[1] XIAOTIAN HUANG,[1,2] BOHAN ZHANG,[1,3,5] DAPING HE,[4] AND SHENGXIANG WANG[1,3,6]

[1] *School of Mathematical and Physical Sciences, Wuhan Textile University, Wuhan 430200, China*
[2] *School of Electronic and Electrical Engineering, Wuhan Textile University, Wuhan 430200, China*
[3] *State Key Laboratory of New Textile Materials and Advanced Processing Technologies, Wuhan Textile University, Wuhan 430200, China*
[4] *Hubei Engineering Research Center of RF-Microwave Technology and Application, Wuhan University of Technology, Wuhan 430070, China*
[5] *bhzhang@wtu.edu.cn*
[6] *shxwang@wtu.edu.cn*

Abstract: We present and numerically verify a functionally hybrid dual-mode tunable polarization conversion metasurface based on graphene and vanadium dioxide (VO$_2$). The tunable polarization converter consists of two patterned graphene layers separated by grating which is composed of gold and VO$_2$. Due to the existence of phase change material VO$_2$, the polarization conversion mode can be switched flexibly between the transmission and reflection modes. Theoretical calculations show the proposed polarization conversion metasurface can obtain giant asymmetric transmission (AT) at 0.42 and 0.77 THz when VO$_2$ is in the insulating state. Conversely, when VO$_2$ is in the metallic state, the converter switches to the reflection mode, demonstrating broadband polarization conversion for both forward and backward incidences. Furthermore, the conductivity of graphene can be modulated by changing the gate voltage, which allows dynamic control polarization conversion bandwidth of the reflection mode as well as the AT of the transmission mode. The robustness of the metasurface has also been verified, the high polarization conversion efficiency and AT can be maintained over wide incidence angles up to 65° for both the *xoz* plane and *yoz* plane. These advantages make the proposed hybrid tunable polarization conversion metasurface a promising candidate for THz radiation switching and modulation.

1. Introduction

Polarization, a fundamental property of electromagnetic waves serves as a crucial information carrier, plays a significant role in the fields of communication and optical polarizer design. However, conventional polarization conversion control methods impose strict material requirements and exhibit limited performance in producing polarization converters. In recent years, metasurfaces have emerged as a promising solution due to their ultra-thin thickness, exceptional performance, and ease of processing [1]. Metasurfaces have been applied in various fields, including antenna communication [2], information coding [3–5], and holographic imaging [6], among others. The dynamic manipulation of metamaterial properties can be accomplished through the modification of the geometrical configuration of metamaterial structures [7–10], or by the alteration of the electromagnetic properties of the constituent components of the metamaterial, such as through continuous [11,12] or structured [13–21] functional layer integration with metal resonators, thereby controlling the symmetry and chirality of the metamaterial-based polarizer during different polarization state transitions.

Recently, tunable THz metasurfaces have garnered attention due to the introduction of phase change materials (PCMs). Several PCMs, including photosensitive silicon [22,23], $Ge_xSb_xTe_x$ (GST) [24–26], vanadium dioxide (VO_2) [27–30], and graphene [31–33]. VO_2, as one of the phase change materials, undergoes a phase change from dielectric to metallic when heated above a critical temperature of 340 K [34–36]. Its corresponding lattice changes from an insulating monoclinic crystalline phase to a metallic rutile phase [37], while its phase change properties can be excited by light fields or thermal radiation. At the same time, the conductivity of VO_2 increases by several orders of magnitude, resulting in a dramatic change in the optoelectronic properties of the device in question. Based on the above characteristics, the introduction of VO_2 materials is attractive for tunable and switchable devices. For instance, VO_2 and graphene materials can change their conductivity by adjusting the external temperature and applying different bias voltages, respectively. In 2018, Zhu [38] et al. designed a dynamically tunable polarization conversion structure through two metal gratings and two orthogonal graphene grating structures, where the polarization state of the structure can be switched by applying different bias voltages to dynamic control the Fermi level of graphene. In 2019, Zhang [39] et al. switch a metamaterial structure between anisotropic 3D-chiral and isotropic achiral configurations, which turn the asymmetry transmission on and off, respectively. In addition, Zhang [40] et al. in 2020 designed switchable chiral mirrors through VO_2 resonant ring and metal ring structures with different opening sizes, the temperature-controlled dielectric-to-metal phase transition of VO_2 has been employed to counteract or eliminate the two-dimensional chirality of the metasurface, enabling the function of spin-orientation switching and on/off switching of circular conversion dichroism. However, most of the above work focuses on conversion efficiency and operating bands in a single mode, lacking the capability to switch between two or more operating modes.

In this work, we present a dual-functional switchable metasurface for converting polarization with high efficiency and controllable reflected/transmitted cross-polarization for the circularly polarized (CP) wave, and the large AT effect of circularly polarized waves can be achieved in transmission. Specifically, at room temperature, the incident CP wave can achieve transmission cross-polarized polarization effect at the response frequency and produce the double-band AT effect. When the room temperature exceeds 340 K, CP waves can be converted into cross-polarized waves over a wide frequency range. Notably, the tunable Fermi energy level of graphene can be used to enhance the response frequency and polarization conversion efficiency. The switchable phase state of VO_2 combined with the tunable Fermi energy level of graphene enables to bring multiple degrees of freedom tuning in operating mode, response frequency and bandwidth, making this metasurface suitable for potential applications in antenna communication, coded imaging, and polarizers.

2. Design and method

The designed multilayer polarization converter based on VO_2 and graphene is shown in Fig. 1. The same horizontally inclined split-ring resonators (SRRs) made of single-layer graphene comprise the top and bottom structures. The upper and lower layers boast uniform spacer thickness made of polyimide (PI) with a dielectric constant of 3.1 [18,20], which yields excellent mechanical, electrical, and chemical stability. The interlayer is a grating composed of Au-VO_2 nanowires with a thickness T of 0.2 μm. The fixed width W of VO_2 is 12 μm, and due to the separation by the Au nanowire, the distance S between them is 22 μm. The entire structure is periodically arranged along the x and y-directions, with each unit period of the device being $P = 120$ μm. The top and bottom graphene resonant rings have an outer radius $R_1 = 48$ μm, an inner radius $R_2 = 38$ μm, and a gap width $L = 14$ μm. The distance between the graphene layer and the grating layer is $H = 58$ μm. The current rapid development of micro and nano processing technology offers the possibility of preparing this metasurface. First, the graphene films are obtained by transferring the graphene monolayer grown by CVD on the copper substrate. Then,

patterned graphene on the top and bottom of the PI film is generated by traditional lithography technology [41]. The surface conductivity of graphene dependent on chemical potential can be continuously changed by adjusting chemical doping or gate voltage in a wide frequency range [42–44]. Next, VO$_2$ and gold gratings with a thickness of 0.2 μm are both prepared by magnetron sputtering, and etching techniques [45].
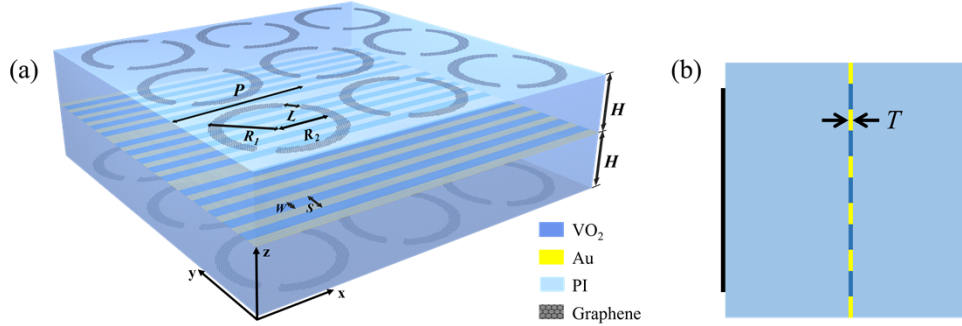

Fig. 1. (a) 3D schematic of a functionally switchable polarization converter, (b) side view.

Then, we calculate reflection parameter S_{11} and transmission parameter S_{21} via the finite-difference time-domain (FDTD) method to evaluate the performance of the designed structure. To simulate an infinite two-dimensional array, we set periodic boundary conditions along the *x* and *y*-directions, while applying perfectly matched layers along the *z*-direction. To improve computational efficiency, graphene can be treated as an infinitely thin two-dimensional sheet due to its thickness of only one atom, simplifying the optical response of its complicated surface conductivity. Such response can be categorized into two groups, in-band contribution and inter-band contribution, which can be characterized by the Kubo formula [46–48]:

$$\sigma(\omega, E_F, \tau, T) = \sigma_{intra}(\omega, E_F, \tau, T) + \sigma_{inter}(\omega, E_F, \tau, T) \tag{1}$$

$$\sigma_{intra}(\omega, E_F, \tau, T) = \frac{2ie^2 k_B T}{\pi \hbar^2 (\omega + i\tau^{-1})} \ln \left[2 \cosh \left(\frac{E_F}{2k_B T} \right) \right] \tag{2}$$

$$\sigma_{inter} = \frac{e^2}{4\hbar} \left[\frac{1}{2} + \frac{1}{\pi} \arctan(\frac{\hbar\omega - 2E_F}{2k_B T}) - \frac{i}{2\pi} \ln \frac{(\hbar\omega + 2E_F)^2}{(\hbar\omega - 2E_F)^2 + 4(k_B T)^2} \right] \tag{3}$$

where *e* is the electron charge, k_B is the Boltzmann constant, *T* is the temperature, $\hbar$ is the reduced Planck's constant, ω is the frequency of the THz wave, τ is the relaxation time of the graphene carrier, and E_F denotes the Fermi level. Functionally as a typical phase change material, VO$_2$ is in the dielectric state at room temperature and in the metallic state above 340 K. In the simulation, the electromagnetic characteristics of VO$_2$ in terahertz band are numerically simulated based on the Drude model, which describes the dielectric constant of VO$_2$ as:

$$\varepsilon(\omega) = \varepsilon_\infty - \frac{\omega_p^2}{\omega^2 + i\gamma\omega} \tag{4}$$

where $\varepsilon_\infty = 12$ represents insulating permittivity at the infinite frequency, $\omega_p(\sigma) = 1.4 \times 10^{15}$ rad/s stands for plasma frequency depending on conductivity, and $\gamma = 5.75 \times 10^{13}$ rad/s indicates the collision frequency [12,49–51]. The relationship between $\omega_p(\sigma_0)$ and conductivity σ is given by the formula $\omega_p^2(\sigma) = \omega_p^2(\sigma_0)\sigma/\sigma_0$, with $\sigma_0 = 3 \times 10^5$ S/m. VO$_2$ exhibits a conductivity of 20 S/m or 2.6×10^5 S/m when in the insulating or metallic phase [27]. Using this formula,

the dielectric constant of VO_2 in the frequency range of 0.1-1.3 THz at different states can be determined, as shown in Fig. 2.

The novel phenomenon of AT is observed when electromagnetic waves pass through a medium in different directions. The giant AT effect in the polarization conversion metasurface is primarily attributed to the synergistic interplay between the polarization conversion effect and the Fabry-Perot-like cavity enhancement effect. For a CP wave, the AT coefficient can be calculated using the following formula [52]:

$$\Delta_{cir}^{+} = |t_{-+}|^2 - |t_{+-}|^2$$
$$\Delta_{cir}^{-} = |t_{+-}|^2 - |t_{-+}|^2 \tag{5}$$
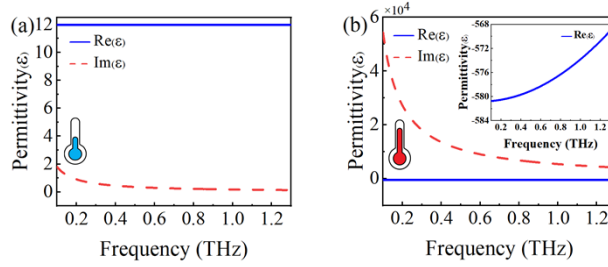

Fig. 2. The permittivity of 0.1-1.3 THz at different conductivity of VO_2 is calculated by the Drude model. (a) Dielectric state and (b) Metallic state.

The transmission coefficients can be defined as: $t_{-+} = E_{-t}/E_{+i}$, $t_{--} = E_{-t}/E_{-i}$, $t_{+-} = E_{+t}/E_{-i}$ and $t_{++} = E_{+t}/E_{+i}$. The CP incident waves the right- and left-handed CP (RCP and LCP) can be replaced by the symbols $+$ and $-$, and the subscripts i and t denote incidence and transmission, respectively. From Eq. (5), it can be easily observed that the significant AT effect is obtained when the transmission coefficients satisfy both $t_{++} = t_{--}$ and $t_{+-} \neq t_{-+}$. In addition, the total energy transmittances of LCP and RCP waves along the forward ($+z$) and backward ($-z$) directions can be expressed using the following equation [53]:

$$T_{+} = |t_{++}|^2 + |t_{+-}|^2$$
$$T_{-} = |t_{--}|^2 + |t_{-+}|^2 \tag{6}$$

3. Results and discussions

3.1. Reflected polarization conversion mode

When the Fermi energy level of graphene E_F is 0.7 eV, and the conductivity of VO_2 is 2.6×10^5 S/m (indicating a metallic state), the Au-VO_2 fence structure in the middle layer can be considered a metallic reflection plane, effectively blocking the propagation of electromagnetic waves. The circularly polarized incident waves can be efficiently converted to cross-polarized waves by the polarization conversion of the double open loops in the upper and lower layers. The cross- and co-polarized coefficients for circular polarization incidence can be defined as: $r_{-+} = E_{-r}/E_{+i}$, $r_{--} = E_{-r}/E_{-i}$, $r_{+-} = E_{+r}/E_{-i}$ and $r_{++} = E_{+r}/E_{+i}$. The CP incident waves LCP and RCP can be replaced by the symbols $+$ and $-$, and the subscripts i and r denote incidence and reflection, respectively. Two sets of reflection coefficients for CP waves incident from the two directions are relatively identical due to the symmetry of the patterned graphene layers. In Figs. 3(a) and 3(b), the co-polarization reflection coefficients $|r_{++}|$ and $|r_{--}|$ are remarkably equal and remain below 0.29 between 0.44-0.9 THz, conversely, the cross-polarization reflection coefficients $|r_{-+}|$ and $|r_{+-}|$ are close to the maximum value of 0.8 in the same operating frequency band. These

results indicate that the designed device achieves the same polarization conversion response under the CP incidence, as the device is 45° aligned with the horizontal plane. Additionally, it is discernible that the cross-polarized reflection coefficients of incident LCP waves were higher than those of incident RCP waves for positive irradiation at 0.44 THz, meanwhile, the opposite was true for backward incident waves. This AT can be ascribed to the fact that the conductivity of metallic VO_2 is slightly lower than Au. To further explicate the conversion efficiency, the polarization conversion rates (PCR) for incident polarized waves can be defined as [54]:

$$PCR_+ = \frac{|r_{-+}|^2}{|r_{++}|^2 + |r_{-+}|^2}$$
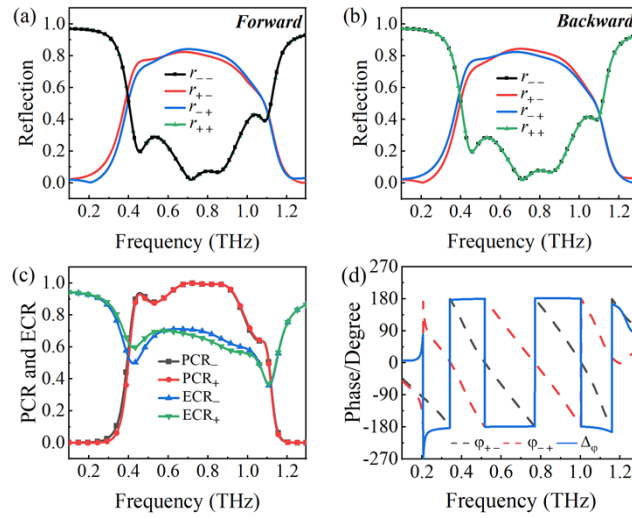$$PCR_- = \frac{|r_{+-}|^2}{|r_{--}|^2 + |r_{+-}|^2}$$

(7)

Fig. 3. Simulated reflection coefficients under (a) Forward incidence and (b) Backward incidence, (c) PCR and ECR for incident circular polarization, (d) Phases.

As depicted in Fig. 3(c), the PCR_+ and PCR_- coefficients are both higher than 0.87 in the range of 0.44-0.9 THz, and were particularly close to 1 in the 0.7-0.87 THz range, indicating the attainment of high efficiency polarization conversion under CP wave incidence. To further evaluate the efficiency of the proposed metasurface, the energy conversion ratio (ECR, $ECR_+ = (|\overrightarrow{E}_-^r|^2 + |\overrightarrow{E}_+^r|^2)/|\overrightarrow{E}_+^i|^2 = |r_{-+}|^2 + |r_{++}|^2$) can be defined under the incident RCP wave. In the frequency range of 0.51–0.8 THz, the ECR curve reaches unity and remains greater than 0.65, proving the substantial energy conversion efficiency in this range. Figure 3(d) shows the phase differences of the reflection coefficients under forward and backward CP waves, where the phase differences of $|r_{+-}|$ and $|r_{-+}|$ tend to stay at approximately $n\pi$ (n is an integer), demonstrating that the metasurface exhibits a nearly perfect reflection symmetry for CP waves.

3.2. Transmission polarization conversion mode

The polarization conversion performances of the transmission CP converter were investigated in Fig. 4, using VO_2 as the insulating dielectric layer, under conditions where the Fermi level E_F of graphene is 0.7 eV and the conductivity of VO_2 is 20 S/m. The fractions of the incident LCP intensity are transmitted as RCP and LCP are given by $|t_{+-}|^2$ and $|t_{--}|^2$, respectively. As depicted in Figs. 4(a) and 4(b), the co-polarization transmission coefficient $|t_{++}|^2 = |t_{--}|^2$, uniformly reaches the minimum value of 0.01 and 0.001 at approximately 0.44 THz and 0.86

THz, respectively, indicating the lack of optical activity. However, significant resonant circular conversion dichroism ($|t_{-+}|^2 \neq |t_{+-}|^2$) was observed at 0.42 THz and 0.77 THz. The maximum values of the CP transmission coefficients are 0.78 and 0.8 when incident LCP waves are approximately 0.42 THz and 0.77 THz, respectively, as shown in Fig. 4(a). The results of the simulation indicate that the designed polarization converter can efficiently convert the incident RCP wave to the LCP wave at 0.42 THz and convert the incident LCP wave to the RCP wave at 0.72 THz for forward incident waves. In contrast, the circular polarization conversion performances for backward incident waves are opposite to those for forward incident waves. At the resonance frequency of 0.42 THz, with incident LCP waves efficiently convert to RCP waves, whereas at 0.77 THz, the efficient conversion of RCP waves to LCP waves is observed, as shown in Fig. 4(b). These results support the potential use of the proposed metamaterial for terahertz devices that require efficient polarization conversion and selection of chiral polarized waves. We calculate PCR and total transmission (T_+ and T_-) using the eigenvalues of Figs. 4(a) and 4(b) to evaluate the efficiency of polarization transmission. The red dotted line in Fig. 4(c) shows that PCR_+ is close to 1 at 0.43 THz and close to 0 at 0.87 THz, whilst the green dotted line represents T_+, which reaches a maximum of 0.66 at 0.74 THz. Similarly, when the LCP wave incident, the black dotted line shows that PCR_- is near 1 at 0.81 THz, reaching the minimum value of 0.01 at 0.44 THz. Meanwhile, the blue dashed line represents T_-, obtaining the maximum value of 0.64 at 0.4 THz. The PCR efficiency demonstrates that the proposed polarization converter can efficiently convert incident RCP/LCP waves into LCP/RCP waves. The total transmission coefficient shows that this converter has a favorable diode effect on CP waves. In the formula (5), since there is no optical activity on the sample side in our case, Δ_{cir} is equal to the total transmission difference between RCP/LCP and LCP/RCP incidences. As shown in Fig. 4(d), the maximum value of Δ_{cir}^- is 0.61 at 0.42 THz, and its minimum value is −0.65 at 0.77 THz, whereas the minimum value of Δ_{cir}^+ is −0.61, and its maximum value at 0.81 THz is 0.65. These results suggest that the proposed polarization converter exhibits a large AT effect for CP waves under both forward and backward incidence.
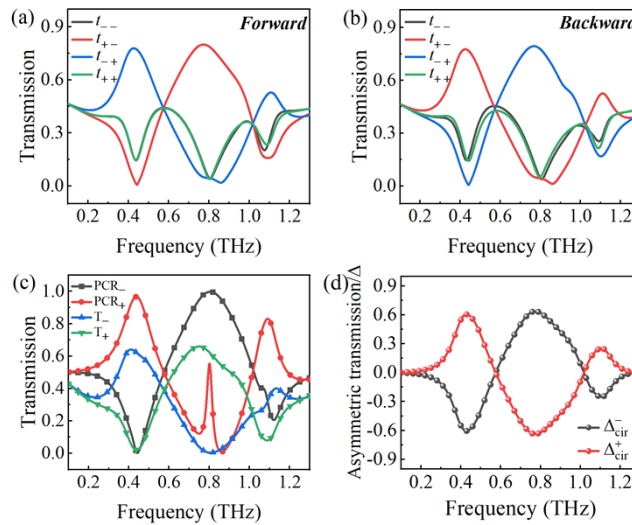

Fig. 4. Simulated transmission coefficients under (a) Forward incidence and (b) Backward incidence, (c) PCR and ECR for incident circular polarization, (d) AT parameters.

To further investigate the AT effect in the proposed polarization converter, we have analyzed the distribution of the surface current. The observed dual-band circular polarization transition phenomenon can be interpreted as the resonant current distribution excited by LCP and RCP

incident on the graphene SRRs, which is revealed by the magnetic field that is perpendicular to the plane of the metamaterial. As shown in Figs. 5(a) and 5(b), when the RCP wave is incident at 0.42 THz, the current on the top graphene resonator is stronger, while the current on the bottom resonator is weaker and flows in the opposite direction. For the LCP wave, the current is strong in both the top and bottom graphene polarizers, meaning that most RCP waves are converted into LCP waves at 0.42 THz, while the incident LCP waves do not undergo polarization conversion upon passing through the structure. Similarly, Figs. 5(c) and 5(d) show that the current in both the top and bottom graphene polarizers is strong at 0.77 THz with RCP wave incidence. Conversely, for the LCP wave, the current on the bottom graphene resonator surface is weaker than that on the top graphene surface, though their current directions are parallel. This implies that at 0.77 THz, the majority of LCP waves are transformed into RCP waves, whereas the incident RCP waves remain unperturbed and do not undergo any polarization conversion upon traversing the structure. These phenomena can be explained by the influence of an electric and magnetic dipole. Specifically, the electric dipole modes are driven by unidirectional currents that effectively radiate and cause polarization transformation of the incident CP wave, producing a rotating field opposite to the incident CP wave. In contrast, the magnetic dipole modes are driven by antisymmetric charge oscillations in the opposite part of the ring, leading to a magnetic moment that is perpendicular to the metamaterial plane. In Fig. 5(a), the surface currents on the top and bottom graphene demonstrate antiparallel phenomena (current flow in the opposite directions), proving that the incident RCP wave incident on the device excites the electric dipole mode and promotes the incident wave to undergo circular polarization conversion ($|t_{-+}|^2$), while the LCP excites the magnetic dipole mode with negligible circular conversion ($|t_{+-}|^2$). On the other hand, the incident LCP waves excite both electric and magnetic dipole modes at 0.77 THz, leading to the polarization conversion of the device at the resonant frequency, which can be demonstrated by parallel currents and a small amount of anti-parallel currents on the two graphene surfaces at both ends.
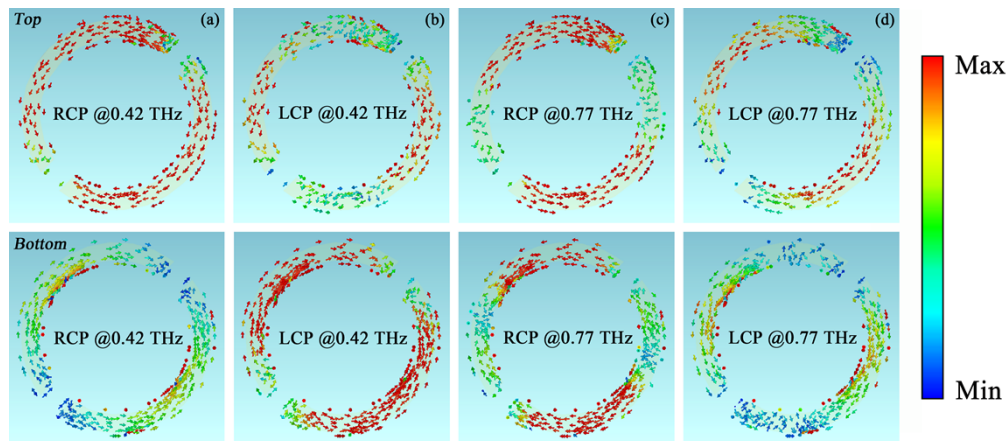

Fig. 5. Simulated surface current densities at 0.42 THz and 0.77 THz transmission for the incident (a, c) RCP and (b, d) LCP waves.

3.3. Dynamic tuning analysis of graphene

In addition to the switchable functions, our design incorporates a feature that allows for dynamic tuning of the polarization conversion efficiency for different functional devices. The conversion of CP waves is recognized to be reliant on the polarization converter's structural parameters, and the converter's function becomes fixed once the device is fabricated. Hence, our device offers a

flexible approach to control the polarization conversion efficiency by dynamically tuning the E_F of graphene. Due to the plasmonic resonance of graphene, the response frequency corresponding to the two polarization transition modes shift slightly blue-shifts with the increase of the E_F, and the bandwidth and intensity of the polarization leap response are affected by it. As shown in Fig. 6(a), as the Fermi level of graphene increases, the cross-polarization reflection coefficients are dynamically tuned from 24% to 86% at 0.42 THz, and $|r_{+-}|$ is dynamically tuned from 0.3% to 84% at 0.7 THz, achieving a tunable broadband effect for circular polarization. Simultaneously, it can be seen that $|r_{+-}|$ decreases rapidly when E_F varies in the range of 0.1~0.3 eV, which is caused by the sudden attenuation of the metallic properties of graphene. In Fig. 6(b), we conducted a simulation where CP waves were forwardly incident, and we adjusted the Fermi level of graphene to assess its impact on the cross-polarization transmission coefficient of the device. Both the cross-polarization coefficient $|t_{+-}|$ and $|t_{-+}|$, undergo a blue-shift in the resonance frequency at 0.34–0.42 THz. However, $|t_{+-}|$ undergoes a dynamic modulation from 60% to 80%, and $|t_{-+}|$ remains relatively stable and close to 0. At 0.64–0.77 THz, the resonant frequency of the incident RCP wave shifts towards the blue end of the spectrum, and $|t_{-+}|$ is modulated in real-time from 68% to 78%, whereas $|t_{+-}|$ remains almost unchanged and close to 0 at its resonant frequency. Therefore, changing the E_F of graphene can effectively tune the CP wave polarization conversion response.
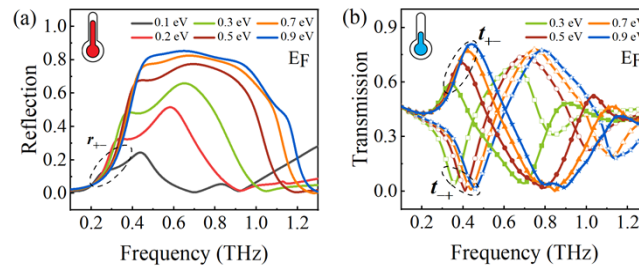

Fig. 6. The effect of E_F modulation on the polarization conversion rate in different modes: (a) reflection mode and (b) transmission mode.

In the last stage of our study, we analyze the variation of the AT effect regarding the Fermi level and oblique incidence. Figures 7(a) and 7(b) show the simulation results of AT coefficients (Δ_{cir}^+ and Δ_{cir}^-) at different Fermi energy levels (0.1~0.7 eV). It can be observed that the E_F has a significant impact on both 0.34–0.42 THz and 0.64–0.77 THz, as the increases of E_F, the resonance frequency is blue-shifted, and the AT coefficient gradually increases at 0.34–0.42 THz. The same phenomenon is observed at 0.64–0.77 THz, although the increment of the AT coefficient is less than that at low frequencies. According to the regulation mechanism of graphene, as the E_F of graphene increases, the metallic properties are gradually enhanced deriving from the increases of the electrical conductivity, resulting in a blue-shift of the resonance frequency. Meanwhile, the effect of electric dipole on the polarization conversion of the incident CP wave increases as the E_F increases, leading to an increase in the AT coefficient. Figures 7(c) and 7(d) demonstrate the negligible impact of controlling the incident angle between 0 and 50° on the AT effect, indicating the device can sustain ideal stability under certain oblique incidence conditions. The results demonstrate that the device can achieve a tunable circular polarization conversion effect under different functions with favorable stability under specific oblique incidence conditions. Our work achieves a deeper understanding of the AT effect in the polarization converter and provides an informed guide for designing similar metasurfaces for various applications.
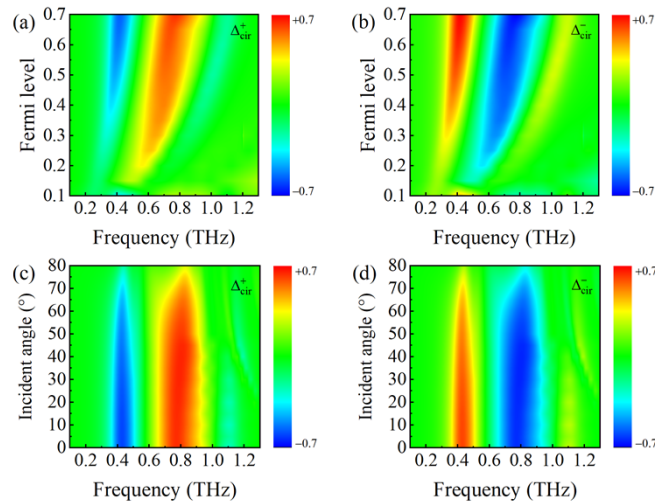
Fig. 7. Dependence of AT (Δ_{cir}^+ and Δ_{cir}^-) on different conditions in the transmission polarization conversion mode: (a, b) E_F, (c, d) incident angles.

4. Conclusion

In this article, we propose a hybrid tunable polarization conversion metasurface by incorporating graphene and VO_2 materials, which can flexibly switch the mode between the transmission and reflection modes. The metasurface can realize a giant AT effect at 0.42 THz and 0.77 THz, achieving the maximum/minimum value of AT as high/low as 0.61/-0.65 when VO_2 retains the insulating state. The inherent symmetry of the structure results in the exhibition of the inverse behavior of AT when a THz wave travels incident from either the forward or backward direction. Furthermore, the metasurface can implement broadband polarization conversion when VO_2 is in the metallic state with PCR_+ and PCR_- coefficients above 0.87 in the range of 0.44–0.9 THz, and the metasurface demonstrates robustness to the incident angles, regardless of whether it operates in transmission or reflection mode. Significantly, our work reveals that the dynamical tunable behavior of the metasurface, such as AT in transmission mode and the polarization conversion in reflection mode, can be facilitated by the introduction of graphene, whose Femi level is amenable to alteration through external stimulus. Considering the ultrafast and flexible dynamic tunable capabilities of VO_2 and graphene, we envision that the proposed hybrid tunable polarization conversion metasurface may provide more degree of freedom for complicated manipulation of THz radiation.

Disclosures. The authors declare no conflicts of interest.

Data availability. Data underlying the results presented in this paper are not publicly available at this time but may be obtained from the authors upon reasonable request.

References

1. A. M. Shaltout, J. Kim, A. Boltasseva, V. M. Shalaev, and A. V. Kildishev, "Ultrathin and multicolour optical cavities with embedded metasurfaces," Nat. Commun. **9**(1), 2673 (2018).
2. A. Clemente, L. Dussopt, R. Sauleau, P. Potier, and P. Pouliguen, "Wideband 400-Element Electronically Reconfig-urable Transmitarray in X Band," IEEE Trans. Antennas Propag. **61**(10), 5017–5027 (2013).
3. F. Shu, J. Wang, R. Peng, B. Xiong, R. Fan, Y. Gao, Y. Liu, D. Qi, and M. Wang, "Electrically Driven Tunable Broadband Polarization States via Active Metasurfaces Based on Joule-Heat-Induced Phase Transition of Vanadium Dioxide," Laser Photonics Rev. **15**(10), 2100155 (2021).
4. L. Zhang, X. Q. Chen, S. Liu, Q. Zhang, J. Zhao, J. Y. Dai, G. D. Bai, X. Wan, Q. Cheng, G. Castaldi, V. Galdi, and T. J. Cui, "Space-time-coding digital metasurfaces," Nat. Commun. **9**(1), 4334 (2018).

5. J. Y. Dai, J. Zhao, Q. Cheng, and T. J. Cui, "Independent control of harmonic amplitudes and phases via a time-domain digital coding metasurface," Light: Sci. Appl. **7**(1), 90 (2018).

6. L. Li, T. Jun Cui, W. Ji, S. Liu, J. Ding, X. Wan, Y. Bo Li, M. Jiang, C. W. Qiu, and S. Zhang, "Electromagnetic reprogrammable coding-metasurface holograms," Nat. Commun. **8**(1), 197 (2017).

7. J. Y. Ou, E. Plum, L. Jiang, and N. I. Zheludev, "Reconfigurable Photonic Metamaterials," Nano Lett. **11**(5), 2142–2144 (2011).

8. W. M. Zhu, A. Q. Liu, X. M. Zhang, D. P. Tsai, T. Bourouina, J. H. Teng, X. H. Zhang, H. C. Guo, H. Tanoto, T. Mei, G. Q. Lo, and D. L. Kwong, "Switchable Magnetic Metamaterials Using Micromachining Processes," Adv. Mater. **23**(15), 1792–1796 (2011).

9. P. Pitchappa, M. Manjappa, C. P. Ho, R. Singh, N. Singh, and C. Lee, "Active Control of Electromagnetically Induced Transparency Analog in Terahertz MEMS Metamaterial," Adv. Opt. Mater. **4**(4), 541–547 (2016).

10. L. Cong, P. Pitchappa, C. Lee, and R. Singh, "Active Phase Transition via Loss Engineering in a Terahertz MEMS Metamaterial," Adv. Mater. **29**(26), 1700733 (2017).

11. L. Liu, L. Kang, T. S. Mayer, and D. H. Werner, "Hybrid metamaterials for electrically triggered multifunctional control," Nat. Commun. **7**(1), 13236 (2016).

12. F. Ding, S. Zhong, and S. I. Bozhevolnyi, "Vanadium Dioxide Integrated Metasurfaces with Switchable Functionalities at Terahertz Frequencies," Adv. Opt. Mater. **6**(9), 1701204 (2018).

13. C. Huang, Y. Feng, J. Zhao, Z. Wang, and T. Jiang, "Asymmetric electromagnetic wave transmission of linear polarization via polarization conversion through chiral metamaterial structures," Phys. Rev. B **85**(19), 195131 (2012).

14. J. Gu, R. Singh, X. Liu, X. Zhang, Y. Ma, S. Zhang, S. A. Maier, Z. Tian, A. K. Azad, H. T. Chen, A. J. Taylor, J. Han, and W. Zhang, "Active control of electromagnetically induced transparency analogue in terahertz metamaterials," Nat. Commun. **3**(1), 1151 (2012).

15. N. K. Grady, J. E. Heyes, D. R. Chowdhury, Y. Zeng, M. T. Reiten, A. K. Azad, A. J. Taylor, D. A. R. Dalvit, and H. T. Chen, "Terahertz Metamaterials for Linear Polarization Conversion and Anomalous Refraction," Science **340**(6138), 1304–1307 (2013).

16. Y. Zhu, S. Vegesna, Y. Zhao, V. Kuryatkov, M. Holtz, Z. Fan, M. Saed, and A. A. Bernussi, "Tunable dual-band terahertz metamaterial bandpass filters," Opt. Lett. **38**(14), 2382 (2013).

17. Q. Lévesque, M. Makhsiyan, P. Bouchon, F. Pardo, J. Jaeck, N. Bardou, C. Dupuis, R. Haïdar, and J. L. Pelouard, "Plasmonic planar antenna for wideband and efficient linear polarization conversion," Appl. Phys. Lett. **104**, 111105 (2014).

18. L. H. Gao, Q. Cheng, J. Yang, S. J. Ma, J. Zhao, S. Liu, H. B. Chen, Q. He, W. X. Jiang, H. F. Ma, Q. Y. Wen, L. J. Liang, B. B. Jin, W. W. Liu, L. Zhou, J. Q. Yao, P. H. Wu, and T. J. Cui, "Broadband diffusion of terahertz waves by multi-bit coding metasurfaces," Light: Sci. Appl. **4**(9), e324 (2015).

19. H. Cai, S. Chen, C. Zou, Q. Huang, Y. Liu, X. Hu, Z. Fu, Y. Zhao, H. He, and Y. Lu, "Multifunctional Hybrid Metasurfaces for Dynamic Tuning of Terahertz Waves," Adv. Opt. Mater. **6**(14), 1800257 (2018).

20. A. Tognazzi, M. Gandolfi, B. Li, G. Ambrosio, P. Franceschini, R. Camacho-Morales, A. C. Cino, C. Baratto, D. de Ceglia, D. Neshev, and C. De Angelis, "Opto-thermal dynamics of thin-film optical limiters based on the VO2 phase transition," Opt. Mater. Express **13**(1), 41–52 (2023).

21. P. Fei, G. A. E. Vandenbosch, W. Guo, X. Wen, D. Xiong, W. Hu, Q. Zheng, and X. Chen, "Versatile Cross-Polarization Conversion Chiral Metasurface for Linear and Circular Polarizations," Adv. Opt. Mater. **8**(13), 2000194 (2020).

22. J. S. Li and X. J. Li, "Switchable tri-function terahertz metasurface based on polarization vanadium dioxide and photosensitive silicon," Opt. Express **30**(8), 12823 (2022).

23. Y. Cui, X. Wang, B. Ren, H. Jiang, and Y. Jiang, "High-efficiency and tunable circular polarization selectivity in photosensitive silicon-based zigzag array metasurface," Opt. Laser Technol. **156**, 108453 (2022).

24. C. H. Chu, M. L. Tseng, J. Chen, P. C. Wu, Y. Chen, H. Wang, T. Chen, W. T. Hsieh, H. J. Wu, G. Sun, and D. P. Tsai, "Active dielectric metasurface based on phase-change medium," Laser Photonics Rev. **10**(6), 986–994 (2016).

25. X. Ding, X. Yang, J. Wang, K. Guo, F. Shen, H. Zhou, R. Sun, Z. Ding, J. Gao, and Z. Guo, "Theoretical analysis and simulation of a tunable mid-infrared filter based on Ge2Sb2Te5 (GST) metasurface," Superlattices Microstruct. **132**, 106169 (2019).

26. C. Choi, S. Mun, J. Sung, K. Choi, S. Lee, and B. Lee, "Hybrid State Engineering of Phase-Change Metasurface for All-Optical Cryptography," Adv. Funct. Mater. **31**(4), 2007210 (2021).

27. M. Liu, E. Plum, H. Li, S. Li, Q. Xu, X. Zhang, C. Zhang, C. Zou, B. Jin, J. Han, and W. Zhang, "Temperature-Controlled Optical Activity and Negative Refractive Index," Adv. Funct. Mater. **31**(14), 2010249 (2021).

28. X. Liu, Q. Wang, X. Zhang, H. Li, Q. Xu, Y. Xu, X. Chen, S. Li, M. Liu, Z. Tian, C. Zhang, C. Zou, J. Han, and W. Zhang, "Thermally Dependent Dynamic Meta-Holography Using a Vanadium Dioxide Integrated Metasurface," Adv. Opt. Mater. **7**(12), 1900175 (2019).

29. S. Yu, Z. Li, W. Liu, H. Cheng, Y. Zhang, B. Xie, W. Zhou, J. Tian, and S. Chen, "Tunable dual-band and high-quality-factor perfect absorption based on VO2-assisted metasurfaces," Opt. Express **29**(20), 31488–31498 (2021).

30. Z. Song, K. Wang, J. Li, and Q. H. Liu, "Broadband tunable terahertz absorber based on vanadium dioxide metamaterials," Opt. Express **26**(6), 7148 (2018).

31. C. He and Z. Song, "Terahertz graphene metasurfaces for cross-polarized deflection, focusing, and orbital angular momentum," Opt. Express **30**(14), 25498–25508 (2022).

32. H. Jung, J. Koo, E. Heo, B. Cho, C. In, W. Lee, H. Jo, J. H. Cho, H. Choi, M. S. Kang, and H. Lee, "Electrically Controllable Molecularization of Terahertz Meta-Atoms," Adv. Mater. **30**(31), 1802760 (2018).

33. Y. Liu, R. Zhong, J. Huang, Y. Lv, C. Han, and S. Liu, "Independently tunable multi-band and ultra-wide-band absorbers based on multilayer metal-graphene metamaterials," Opt. Express **27**(5), 7393–7404 (2019).

34. O. L. Muskens, L. Bergamini, Y. Wang, J. M. Gaskell, N. Zabala, C. De Groot, D. W. Sheel, and J. Aizpurua, "Antenna-assisted picosecond control of nanoscale phase transition in vanadium dioxide," Light: Sci. Appl. **5**(10), e16173 (2016).

35. A. Tripathi, J. John, S. Kruk, Z. Zhang, H. S. Nguyen, L. Berguiga, P. R. Romeo, R. Orobtchouk, S. Ramanathan, Y. Kivshar, and S. Cueff, "Tunable Mie-Resonant Dielectric Metasurfaces Based on VO$_2$ Phase-Transition Materials," ACS Photonics **8**(4), 1206–1213 (2021).

36. B. Li, R. Camacho-Morales, N. Li, A. Tognazzi, M. Gandolfi, D. De Ceglia, C. De Angelis, A. A. Sukhorukov, and D. N. Neshev, "Fundamental limits for transmission modulation in VO$_2$ metasurfaces," Photonics Res. **11**(1), B40 (2023).

37. Y. G. Jeong, S. Han, J. Rhie, J. S. Kyoung, J. W. Choi, N. Park, S. Hong, B. J. Kim, H. T. Kim, and D. S. Kim, "A Vanadium Dioxide Metamaterial Disengaged from Insulator-to-Metal Transition," Nano Lett. **15**(10), 6318–6323 (2015).

38. Y. Zhang, Y. Feng, T. Jiang, J. Cao, J. Zhao, and B. Zhu, "Tunable broadband polarization rotator in terahertz frequency based on graphene metamaterial," Carbon **133**, 170–175 (2018).

39. M. Liu, Q. Xu, X. Chen, E. Plum, H. Li, X. Zhang, C. Zhang, C. Zou, J. Han, and W. Zhang, "Temperature-Controlled Asymmetric Transmission of Electromagnetic Waves," Sci. Rep. **9**(1), 4097 (2019).

40. M. Liu, E. Plum, H. Li, S. Duan, S. Li, Q. Xu, X. Zhang, C. Zhang, C. Zou, B. Jin, J. Han, and W. Zhang, "Switchable Chiral Mirrors," Adv. Opt. Mater. **8**(15), 2000247 (2020).

41. R. Zhang, J. Fu, H. Wang, X. Wei, X. Li, and H. Shi, "In-Situ Growth of High-Quality Customized Monolayer Graphene Structures for Optoelectronics," Adv. Funct. Mater. **32**(42), 2202376 (2022).

42. S. Wang, H. Liu, J. Tang, M. Chen, Y. Zhang, J. Xu, T. Wang, J. Xiong, H. Wang, Y. Cheng, S. Qu, and L. Yuan, "Tunable and switchable bifunctional meta-surface for plasmon-induced transparency and perfect absorption," Opt. Mater. Express **12**(2), 560 (2022).

43. Z. Chen, X. Li, J. Wang, L. Tao, M. Long, S. J. Liang, L. K. Ang, C. Shu, H. K. Tsang, and J. B. Xu, "Synergistic Effects of Plasmonics and Electron Trapping in Graphene Short-Wave Infrared Photodetectors with Ultrahigh Responsivity," ACS Nano **11**(1), 430–437 (2017).

44. J. Wang, B. Xiong, R. Peng, C. Li, B. Hou, C. Chen, Y. Liu, and M. Wang, "Flexible Phase Change Materials for Electrically-Tuned Active Absorbers," Small **17**(31), 2101282 (2021).

45. A. D. Squires, X. Gao, J. Du, Z. Han, D. H. Seo, J. S. Cooper, A. T. Murdock, S. K. H. Lam, T. Zhang, and T. Van Der Laan, "Electrically tuneable terahertz metasurface enabled by a graphene/gold bilayer structure," Commun. Mater. **3**(1), 56 (2022).

46. M. Jablan, H. Buljan, and M. Soljačić, "Plasmonics in graphene at infrared frequencies," Phys. Rev. B **80**(24), 245435 (2009).

47. J. Horng, C. F. Chen, B. Geng, C. Girit, Y. Zhang, Z. Hao, H. A. Bechtel, M. Martin, A. Zettl, M. F. Crommie, Y. R. Shen, and F. Wang, "Drude conductivity of Dirac fermions in graphene," Phys. Rev. B **83**(16), 165113 (2011).

48. S. H. Lee, M. Choi, T. T. Kim, S. Lee, M. Liu, X. Yin, H. K. Choi, S. S. Lee, C. G. Choi, S. Y. Choi, X. Zhang, and B. Min, "Switching terahertz waves with gate-controlled active graphene metamaterials," Nat. Mater. **11**(11), 936–941 (2012).

49. M. Liu, H. Y. Hwang, H. Tao, A. C. Strikwerda, K. Fan, G. R. Keiser, A. J. Sternbach, K. G. West, S. Kittiwatanakul, J. Lu, S. A. Wolf, F. G. Omenetto, X. Zhang, K. A. Nelson, and R. D. Averitt, "Terahertz-field-induced insulator-to-metal transition in vanadium dioxide metamaterial," Nature **487**(7407), 345–348 (2012).

50. S. Wang, L. Kang, and D. H. Werner, "Hybrid Resonators and Highly Tunable Terahertz Metamaterials Enabled by Vanadium Dioxide (VO2)," Sci. Rep. **7**(1), 4326 (2017).

51. W. Liu and Z. Song, "Terahertz absorption modulator with largely tunable bandwidth and intensity," Carbon **174**, 617–624 (2021).

52. X. Jing, X. Gui, P. Zhou, and Z. Hong, "Physical Explanation of Fabry–Pérot Cavity for Broadband Bilayer Metamaterials Polarization Converter," J. Lightwave Technol. **36**(12), 2322–2327 (2018).

53. F. Yu, J. Zhu, and X. Shen, "Tunable and reflective polarization converter based on single-layer vanadium dioxide-integrated metasurface in terahertz region," Opt. Mater. **123**, 111745 (2022).

54. J. S. Li and F. Q. Bai, "Dual-band terahertz polarization converter with high-efficiency asymmetric transmission," Opt. Mater. Express **10**(8), 1853–1861 (2020).